Multiple-fringe structure of attosecond transient absorption spectrum driven by mid-infrared laser

Jinxing Xue (薛金星)[1,2,3], Candong Liu (刘灿东)[1,2,*], Zhinan Zeng (曾志男)[1,2,], Ruxin Li (李儒新)[1,2], and Zhizhan Xu (徐至展)[1]**

[1]*Shanghai Institute of Optics and Fine Mechanics, Chinese Academy of Sciences, Shanghai 201800, China*
[2]*Center of Materials Science and Optoelectronics Engineering, University of Chinese Academy of Sciences, Beijing 100049, China*
[3]*University of Chinese Academy of Sciences, Beijing 100049, China*
**Corresponding author: cdliu@siom.ac.cn; **corresponding author: zhinan_zeng@mail.siom.ac.cn*
Received April 9, 2019; accepted May 14, 2019; posted online July 23, 2019

We theoretically investigate the delay-dependent attosecond transient absorption spectra in the helium atom dressed by an infrared laser pulse in the wavelength range of 800–2400 nm. By numerically solving the three-dimensional time-dependent Schrödinger equation, we find that the absorption spectrogram exhibits a multiple-fringe structure for using the mid-infrared dressing pulse. The quantitative calculation of the transition matrix between different Floquet states provides direct evidence on the origin of the multiple-fringe structure. Our result shows that the wavelength of the dressing pulse is an important parameter and the unique feature of attosecond transient absorption spectroscopy can be induced in the mid-infrared regime.

OCIS codes: 260.3090, 300.1030, 340.7480.
doi: 10.3788/COL201917.082601.

The development of attosecond transient absorption spectroscopy (ATAS) in recent years[1–8] has benefited from the advent of attosecond extreme ultraviolet (XUV) pulse, which paves the way for progress in the investigation of ultrafast dynamics of electrons on their natural time scale[1,9–16]. The pump-probe scheme is usually implemented in ATAS, where whether the XUV and infrared (IR) pulse serves as a pump or probe depends on the specific situation. The pump pulse initiates the dynamics of electrons, and the time-delayed probe pulse is used to read out the information of the dynamical process by measuring the transmitted spectrum of the XUV pulse. The high temporal and spectral resolution enables ATAS to be an important tool for studying complex electronic processes. For example, ATAS has been used to study laser-induced electron dynamics of bound states and low-energy continuum states in atoms and molecules[2,3,5–7,17–21], including the observation of the AC Stark effect[5] and sub-cycle absorption of virtual states in laser-dressed helium atoms[7]. The transformation of the asymmetric Fano spectral absorption lines into symmetric Lorentzian absorption peaks in doubly excited helium and vice versa, and from Lorentzian to Fano in singly excited helium[22], have been investigated. Moreover, the reshaping effect[23] and the chirp effect[24] of an XUV pulse on the transient absorption have been theoretically studied. ATAS has also been successfully applied to solid matter. The dynamic properties of valence and conduction bands in silicon have been experimentally studied[25–27].

In general, most of the works on ATAS are based on 800 nm near infrared (NIR) wavelength lasers, where ATAS mainly has one absorption signal in one half cycle of NIR laser. If the driving laser wavelength is increased to the mid-infrared (MIR, ~2400 nm) range, the electron will experience more time within one optical cycle, which can accumulate a larger phase. Consequently, some new features and dynamic process may emerge. To explore this new parameter regime, we numerically calculate the ATAS of a singly excited helium atom under MIR and attosecond XUV pulses. By varying the time delay between the two pulses, we find a feature of grouped multiple fringes in the ATAS. As the wavelength of the dressing laser pulse varies from 800 nm to 2400 nm, the number of absorption peaks in each group increases.

The three-dimensional time-dependent Schrödinger equation (3D–TDSE) under single active electron approximation is used to simulate the absorption spectrum of helium atom. A detailed description of this 3D-TDSE can be found in reference[24].

The dipole can be calculated as $d(t) = \langle \psi(t)|x|\psi(t)\rangle$. Here, $|\psi(t)\rangle$ is the time-dependent wave function of electron and x is a position operator. This time-dependent dipole is driven by the total electric field comprising the MIR and XUV pulses, representing the response of an electron to an external electric field. The Fourier transform of this dipole oscillation yields the dipole spectrum $d(\Omega, \tau)$, from which the ATAS can be written as[23,28] $S(\Omega, \tau) = 2\mathrm{Im}[d^*(\Omega, \tau)E(\Omega)]$, $\Omega \geq 0$. Here, τ is the time delay between the MIR and XUV pulses, and $E(\Omega)$ is the spectrum of the XUV pulse. The positive (negative) value of $S(\Omega, \tau)$ is the absorption (emission) of light at frequency Ω.

The intensity of the isolated XUV pulse used in our simulation is 0.1 TW/cm^2, which can be easily obtained from high harmonic generation. The central photon energy of the XUV pulse is 21 eV, and its transform-limited duration is 300 as, resulting in a bandwidth of 6 eV.

The bandwidth of this XUV pulse can cover all the excited states below the ionization threshold ($I_P = 24.6$ eV). To avoid the nonlinear effect of the MIR field, a relatively weak MIR pulse is used.

The ATAS calculated for laser wavelengths of 800 nm and 2400 nm is shown in Figs. 1(a) and 1(c), respectively. The duration of the IR (MIR) laser pulse used in the simulation is four optical cycles (O.C.). The laser intensity is fixed at 5 TW/cm^2. The positive (negative) delay means that the XUV pulse arrives after (before) the MIR pulse. Features like the AC Stark effect and the laser-induced states (LIS) in the previous work can be clearly observed in Figs. 1(a) and 1(c). In this work, the LIS $2s^-$ and $2p^{2-}$ are chosen for analysis because these two states are far away from higher excited states so that the effects of the higher excited states can be ignored. The notation $2s^-$ means that the LIS energy is one-laser-photon energy below the atomic eigenstate 2s. In Fig. 1(c), the energies of the LIS $2s^-$ and $2p^{2-}$ are indicated by the white-dashed lines. The energies of the 2p, 3p, and $2s^+$ states are also labeled on the left side in Fig. 1(a). For the case of 800 nm, the absorptions located at $2s^-$ and $2p^{2-}$ are about one order of magnitude smaller than that located at 2p. For better visualization, the ATAS around $2s^-$ and $2p^{2-}$ is enlarged, as shown in Fig. 1(b) with a different color scale. In Fig. 1(b), the ATAS around $2s^-$ is half-cycle modulated (only one fringe in one half-cycle) along the delay axis, while for 2400 nm in Fig. 1(c) the ATAS around $2s^-$ exhibits a multiple-fringe structure, forming the group feature spaced by a half optical cycle. Here, a group feature means that more than one absorption peak is grouped together within one half-cycle delay, as shown by the lower white-dashed lines in Fig. 1(c). For the ATAS located at $2p^{2-}$, there is no group feature for both wavelengths, viz., 800 nm and 2400 nm, as shown in Figs. 1(b) and 1(c), respectively.

As reported in previous work[4,28], the 2ω and 4ω oscillation frequencies of the absorption signals can be observed at some specific positions. In our work, we quantitatively investigate the oscillation strength of the 2ω, 4ω, and 6ω components of LIS $2s^-$ and $2p^{2-}$ dependent on the dressing laser wavelength by performing a Fourier transformation along the delay axis. To make it clear, we take the 2ω component as reference, and the relative strengths of 4ω and 6ω components can be obtained as a function of laser wavelength, as shown in Figs. 2(a) and 2(b). In Fig. 2(a), we can clearly see the increase of the 4ω component with the increase of the laser wavelength. To draw a quantitative comparison, the relative strengths for the 2ω (blue-solid), 4ω (red-dot), and 6ω (carmine-dashed) components are plotted in Figs. 2(c) and 2(d).

In Fig. 2(c), one can see that the 4ω component is stronger than the 2ω component when the wavelength reaches 2400 nm. Around this wavelength, the group feature can be clearly observed, as shown in Fig. 1(c). The 6ω component can be ignored due to its small value, but it is still increasing. For the $2p^{2-}$ shown in Fig. 2(d), the 4ω and 6ω components are much smaller than the 2ω component, which makes the multiple fringe structure unclear in Fig. 1(c).

As mentioned above, the 3D-TDSE model has shown the high-frequency oscillation of the ATAS dependent on the laser wavelength; we still need the Floquet theory to uncover the role of the MIR and XUV pulses in the ATAS. First, in the Floquet picture, the interaction between the MIR field and the atom is considered as a unified eigensystem, forming a series of dressed states (Floquet states) in which the energies for a group of Floquet states originating from the same field-free atomic state are separated by one MIR photon. Second, the XUV pulse interacts with the new generated system by pushing the ground-state electron into different Floquet states within the spectrum of the XUV pulse. The concept of Floquet states is very useful for analyzing the LISs

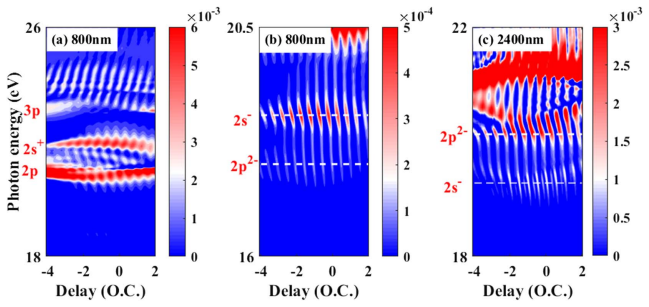

Fig. 1. ATAS calculated for (a) 800 nm and (c) 2400 nm laser pulses with 3D-TDSE. For better observation, the region in (a) with the photon energy ranging from 16 to 20.5 eV is enlarged in (b). In (b) and (c), the absorption signals for $2s^-$ and $2p^{2-}$ are marked by white-dashed lines.

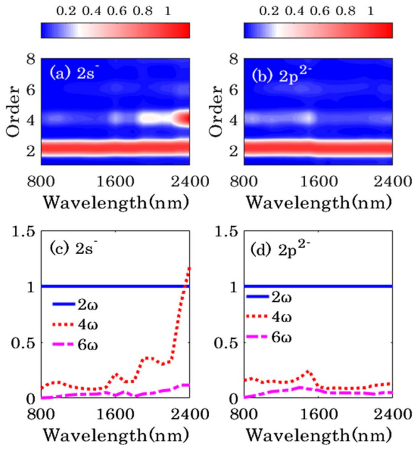

Fig. 2. Relative oscillation strength of the 2ω, 4ω, and 6ω components calculated from the 3D-TDSE as a function of the dressing laser wavelength. (a) and (c) show the result for the $2s^-$ state. (b) and (d) show the result for the $2p^{2-}$ state. In (c) and (d), the blue solid lines indicate the strength of the 2ω component as reference, while the red-dot and the carmine-dashed lines represent the 4ω and 6ω components, respectively.

occurring in the transient absorption. The ideas and notations in this section follow the work of Wu *et al.*[28].

In the Floquet theory, the Floquet Hamiltonian is expanded in the direct product of atomic states $|\alpha\rangle$ and the 'Fourier basis' $|m\rangle$ as

$$\langle\alpha, n|H_F|\beta, m\rangle = (\varepsilon_\beta - m\omega)\delta_{\alpha,\beta}\delta_{n,m} + \frac{1}{2}d_{\alpha\beta}(\delta_{n+1,m} + \delta_{n,m+1}). \quad (1)$$

Here, H_F is the Floquet Hamiltonian, $|\alpha, m\rangle = |\alpha\rangle \otimes |m\rangle = |\alpha\rangle e^{-im\omega t}$, and these "Fourier bases" can also be understood as the photon number basis. The symbol $\otimes$ denotes the direct product. $d_{\alpha\beta}$ denotes the transition elements between the atomic states $|\alpha\rangle$ and $|\beta\rangle$. After diagonalizing the Floquet matrix [Eq. (1)], the time-independent Floquet state $|\phi_{\alpha,m}\rangle$ and its energy can be obtained. Once the electronic wave function is constructed from these time-independent Floquet states, the dipole oscillation induced by the quantum beat between different Floquet states and the ground state can be written as[28]

$$D(t,\tau) = \sum_{\alpha,n,m} e^{-i(\varepsilon_\alpha + m\omega)t} e^{i(n-m)\omega\tau}\langle\phi_{\alpha,n}|\mu_X|\psi_0\rangle\langle\psi_0|\mu_X|\phi_{\alpha,m}\rangle + \text{c.c.} \quad (2)$$

Here, ε_α is the Floquet energy, $|\psi_0\rangle$ is the ground state, and τ is the pump-probe delay. μ_X is the dipole operator of the XUV pulse, meaning that the dipole described by Eq. (2) is only induced by the XUV pulse. This time-dependent dipole oscillation can be used to analyze the features of the absorption spectrum.

The Floquet theory has already been used to analyze the absorption process in ATAS[28,29]. This is because the Floquet state $|\alpha, m\rangle$ is equivalent to LIS α^m and can be analytically or numerically obtained. In what follows, we only focus on the absorption signals for the $2s^-$ and $2p^{2-}$ states.

We use three atomic states, viz., 1s, 2s, and 2p, as the basis, and 13 Floquet ladders for each atomic state, which is large enough to describe the absorption process accurately. According to Eq. (2), the time- and delay-dependent dipole, which describes the absorption at energy position $\varepsilon_\alpha + m\omega$, can be written as

$$d(t,\tau) = \sum_{n} e^{-i(\varepsilon_\alpha + m\omega)t} e^{i(n-m)\omega\tau}\langle\phi_{\alpha,n}|\mu_X|\psi_0\rangle\langle\psi_0|\mu_X|\phi_{\alpha,m}\rangle + \text{c.c.} \quad (3)$$

The Fourier transformation of this time-dependent dipole gives the dipole spectrum. Substituting this dipole spectrum into the response function, ignoring the spectrum profile of the electric field, and setting the spectrum phase of the electric field to be $\pi/2$, the response function can be written as

$$S(\Omega,\tau) = 2\delta[\Omega - (\varepsilon_\alpha + m\omega)]\langle\psi_0|\mu_X|\phi_{\alpha,m}\rangle g(\tau). \quad (4)$$

Here, $\delta[\Omega - (\varepsilon_\alpha + m\omega)]$ is a delta function corresponding to the absorption located at $|\alpha, m\rangle$ (or LIS α^m). $g(\tau) = \langle\psi_0|\mu_X|\phi_{\alpha,m}\rangle\sum_p\langle\phi_{\alpha,m+2p}|\mu_X|\psi_0\rangle\cos(2p\omega\tau)$ is the modulation function, and $p = 0, \pm1, \pm2, \pm3, \ldots$ represents $0\omega, 2\omega, 4\omega, 6\omega, \ldots$ modulation. In Eq. (4), the transition element $\langle\psi_0|\mu_X|\phi_{\alpha,m}\rangle$ determines the strength of absorption at the energy position $\varepsilon_\alpha + m\omega$. The modulation function $g(\tau)$ can be written more explicitly in the form

$$\begin{aligned} g(\tau) = {} & \langle\phi_{\alpha,m}|\mu_X|\psi_0\rangle\cos(0\omega\tau) \\ & + [\langle\phi_{\alpha,m-2}|\mu_X|\psi_0\rangle + \langle\phi_{\alpha,m+2}|\mu_X|\psi_0\rangle]\cos(2\omega\tau) \\ & + [\langle\phi_{\alpha,m-4}|\mu_X|\psi_0\rangle + \langle\phi_{\alpha,m+4}|\mu_X|\psi_0\rangle]\cos(4\omega\tau) \\ & + [\langle\phi_{\alpha,m-6}|\mu_X|\psi_0\rangle + \langle\phi_{\alpha,m+6}|\mu_X|\psi_0\rangle]\cos(6\omega\tau) + \ldots . \end{aligned} \quad (5)$$

It should be noted that the 0ω component in Eq. (5) gives a basis for the absorption signals. In addition, it is clear that the strength of the 2ω oscillation is determined by the sum of two transition matrix elements $\langle\phi_{\alpha,m-2}|\mu_X|\psi_0\rangle$ and $\langle\phi_{\alpha,m+2}|\mu_X|\psi_0\rangle$, physically meaning that two quantum paths interfere. The two involved quantum states are $|\phi_{\alpha,m-2}\rangle$ and $|\phi_{\alpha,m+2}\rangle$. For instance, the oscillation strength of the 2ω component for $|2s,-1\rangle$ is determined by the interference of quantum paths from $|2s,-3\rangle$ and $|2s,+1\rangle$. This result disagrees with previous work where the 2ω oscillation of $|2s,-1\rangle$ is attributed to the interference from quantum paths $|2s,-1\rangle$ and $|2s,+1\rangle$[28]. For convenience, Eq. (5) can be rewritten as $g(\tau) = g_0\cos(0\omega\tau) + g_1\cos(2\omega\tau) + g_2\cos(4\omega\tau) + g_3\cos(6\omega\tau) + \ldots$. Here, $g_0 = \langle\phi_{\alpha,m}|\mu_X|\psi_0\rangle$ and $g_i = \langle\phi_{\alpha,m-2i}|\mu_X|\psi_0\rangle + \langle\phi_{\alpha,m+2i}|\mu_X|\psi_0\rangle$, $i = 1, 2, 3, \ldots$. When taking g_1 as reference, the modulation function can be reduced to

$$f(\tau) = f_0\cos(0\omega\tau) + f_1\cos(2\omega\tau) + f_2\cos(4\omega\tau) + f_3\cos(6\omega\tau) + \ldots . \quad (6)$$

Here, $f_i = g_i/g_1$, $i = 0, 1, 2, \ldots$. Except for f_0, the other coefficients f_1, f_2, and f_3 can be called modulation coefficients as they represent the relative modulation strength of the 2ω, 4ω, and 6ω modulation components. Usually, the coefficient f_1 is maximum, resulting in the strongest 2ω modulation. For instance, for a laser pulse with a wavelength of $\lambda = 800$ nm and intensity $I_0 = 5$ TW/cm^2, the modulation coefficients f_1, f_2, and f_3 for the Floquet state $|2s,-1\rangle$ are $f_1 = 1$, $f_2 = 0.013$, and $f_3 = 0.0005$. Obviously, $f_1 > f_2 > f_3$, and the 2ω modulation will be dominant in ATAS. This is indeed the case, as it can be seen from Fig. 1(b) that only the half-cycle modulation at $|2s,-1\rangle$ is visible. It is therefore found that, from Eq. (6), the modulation function $f(\tau)$ describes the group features in ATAS. To confirm this conclusion further, the modulation coefficients f_1, f_2, and f_3 are calculated upon scanning the wavelengths from 800 nm to 2400 nm. The laser intensity is kept the same as that in Fig. 2.

In Figs. 3(a) and 3(b), the modulation coefficients f_1 (black-square), f_2 (red-cycle), and f_3 (blue-triangle) are calculated for the absorption lines at Floquet states $|2s,-1\rangle$ and $|2p,-2\rangle$, respectively. Comparing the results shown in Fig. 3(a) with those in Fig. 2(c), we identify that the modulation coefficients calculated through the Floquet theory have successfully revealed the relative strength of the 2ω, 4ω, and 6ω modulation frequency for $|2s,-1\rangle$. The same conclusion can be drawn for $|2p,-2\rangle$ from the results shown in Figs. 3(b) and 2(d). In Fig. 3(a), when the laser wavelength is shorter than 2000 nm, the coefficient f_2 is much smaller than f_1, meaning that the 2ω modulation is dominating and the group feature cannot be observed in ATAS. With increasing wavelength, f_2 becomes comparable to f_1, which means that the 2ω modulation is no longer dominant, causing the appearance of the group feature in ATAS. When the wavelength is tuned to 2400 nm, f_2 is even greater than f_1. Therefore, the 4ω modulation is dominant, resulting in two absorption peaks in one group, as shown in Fig. 1(c). The coefficient f_3 increases slowly with increasing wavelength, but it is still too small to affect the absorption process. In Fig. 3(b) the coefficients f_2 and f_3 are both smaller than f_1; hence, the group feature is invisible. It should be noted that the MIR laser pulse is a monochromatic plane wave and the XUV pulse is assumed to be a delta function temporally in the ATAS Floquet theory. The agreement between Fig. 3 and Fig. 2 confirms that the Floquet theory can shed light on the multiple fringe structure of the ATAS very well.

In conclusion, our work presents a theoretical simulation of the ATAS of the helium atom, with emphasis on the wavelength of the dressing laser pulse in the MIR range. Two methods, viz., the 3D-TDSE and the Floquet theory, are used to reveal the novel characteristics of the ATAS of the helium atom. We find that the absorption spectrum shows a structure of grouped multiple fringes that are dependent on the laser wavelength. Using the Floquet theory, we confirm that the grouped structures are the result of the superposition of different oscillation components, and the number of absorption peaks in each group is determined by the relative value of the transition matrix from the ground state to relevant Floquet states. For the 2400 nm laser, two absorption peaks are grouped together. In addition to the AC Stark effect and the non-adiabatic effect, this group feature is a prominent feature in ATAS when the laser wavelength is tuned to the MIR.

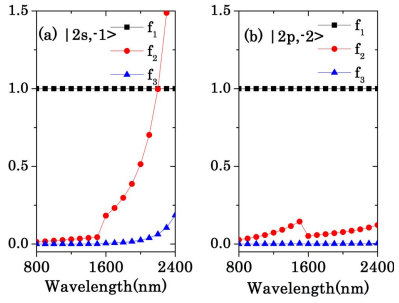

Fig. 3. Modulation coefficients f_1, f_2, and f_3 as a function of wavelength for two different Floquet states: (a) $|2s,-1\rangle$ and (b) $|2p,-2\rangle$. The dressing laser intensity is the same as that in Fig. 2. The black-square, red-cycle, and blue-triangle lines represent the modulation coefficients f_1, f_2, and f_3, respectively.

This work was supported by the National Natural Science Foundation of China (Nos. 61690223, 11774363, 11561121002, 61521093, 11127901, 11227902, and 11574332), the Strategic Priority Research Program of the Chinese Academy of Sciences (No. XDB16), and the Youth Innovation Promotion Association CAS.

References

1. R. Krupa, R. L. Stephen, and M. N. Daniel, Annu. Rev. Phys. Chem. **67**, 41 (2016).
2. H. Wang, M. Chini, S. Y. Chen, C. H. Zhang, F. He, Y. Cheng, Y. Wu, U. Thumm, and Z. H. Chang, in *CLEO* (OSA, 2011), paper QMG3.
3. Y. Cheng, M. Chini, X. M. Tong, A. Chew, J. Biedermann, Y. Wu, E. Cunningham, and Z. H. Chang, in *CLEO* (OSA, 2015), paper FTh3C.3.
4. M. Chini, X. W. Wang, Y. Cheng, and Z. H. Chang, J. Phys. B **47**, 124009 (2014).
5. M. Chini, B. Z. Zhao, H. Wang, Y. Cheng, S. X. Hu, and Z. H. Chang, Phys. Rev. Lett. **109**, 073601 (2012).
6. X. W. Wang, M. Chini, Y. Cheng, Y. Wu, X. M. Tong, and Z. H. Chang, Phys. Rev. A **87**, 063413 (2013).
7. M. Chini, X. M. Wang, Y. Cheng, Y Wu, D Zhao, D. A. Telnov, S. I. Chu, and Z. H. Chang, Sci. Rep. **3**, 1105 (2013).
8. M. Chini, X. W. Wang, Y. Cheng, H. Wang, Y. Wu, E. Cunningham, P. C. Li, J. Heslar, D. A. Telnov, S. I. Chu, and Z. H. Chang, Nat. Photonics **8**, 437 (2014).
9. A. R. Beck, M. N. Daniel, and R. L. Stephen, Chem. Phys. Lett. **624**, 119 (2015).
10. E. R. Warrick, W. Cao, D. M. Neumark, and S. R. Leone, J. Phys. Chem. A **120**, 3165 (2016).
11. J. E. Baekhoj, L. Yue, and L. B. Madsen, Phys. Rev. A **91**, 14 (2015).
12. M. Reduzzi, W. C. Chu, C. Feng, A. Dubrouil, J. Hummert, F. Calegari, F. Frassetto, L. Poletto, O. Kornilov, M. Nisoli, C. D. Lin, and G. Sansone, J. Phys. B **49**, 065102 (2016).
13. L. Argenti, Á. Jiménez-Galán, C. Marante, C. Ott, T. Pfeifer, and F. Martín, Phys. Rev. A **91**, 061403 (2015).
14. Z. Q. Yang, D. F. Ye, T. Ding, T. Pfeifer, and L. B. Fu, Phys. Rev. A **91**, 013414 (2015).
15. W. P. Dong, Y. Q. Li, X. W. Wang, J. M. Yuan, and Z. X. Zhao, Phys. Rev. A **92**, 033412 (2015).
16. F. He, C. Ruiz, A. Becker, and U. Thumm, J. Phys. B **44**, 211001 (2011).
17. E. Goulielmakis, Z. H. Loh, A. Wirth, R. Santra, N. Rohringer, V. S. Yakovlev, S. Zherebtsov, T. Pfeifer, A. M. Azzeer, M. F. Kling, S. R. Leone, and F. Krausz, Nature **466**, 739 (2010).
18. P. Stefan, S. Arina, M. Antoine, W. Adrian, G. Eleftherios, and S. Robin, Phys. Rev. A **86**, 063411 (2012).
19. A. Wirth, M. Th. Hassan, I. Grguraš, J. Gagnon, A. Moulet, T. T. Luu, S. Pabst, R. Santra, Z. A. Alahmed, A. M. Azzeer, V. S. Yakovlev, V. Pervak, F. Krausz, and E. Goulielmakis, Science **334**, 195 (2011).
20. S. H. Chen, M. J. Bell, A. R. Beck, H. Mashiko, M. X. Wu, A. N. Pfeiffer, M. B. Gaarde, D. M. Neumark, S. R. Leone, and K. J. Schafer, Phys. Rev. A **86**, 063408 (2012).

21. S. H. Chen, M. X. Wu, M. B. Gaarde, and K. J. Schafer, Phys. Rev. A **87**, 033408 (2013).
22. C. Ott, A. Kaldun, P. Raith, K. Meyer, M. Laux, J. Evers, C. H. Keitel, C. H. Greene, and T. Pfeifer, Science **340**, 716 (2013).
23. M. B. Gaarde, C. Buth, J. L. Tate, and K. J. Schafer, Phys. Rev. A **83**, 013419 (2011).
24. H. W. Zhao, C. D. Liu, Y. H. Zheng, Z. N. Zeng, and R. X. Li, Opt. Express **25**, 7707 (2017).
25. M. Schultze, E.M. Bothschafter, A. Sommer, S. Holzner, W. Schweinberger, M. Fiess, M. Hofstetter, R. Kienberger, V. Apalkov, V. S. Yakovlev, M. I. Stockman, and F. Krausz, Nature **493**, 75 (2012).
26. M. Schultze, K. Ramasesha, C. D. Pemmaraju, S. A. Sato, D. Whitmore, A. Gandman, J. S. Prell, L. J. Borja, D. Prendergast, K. Yabana, D. M. Neumark, and S. R. Leone, Science **346**, 1348 (2014).
27. M. Sabbar, H. Timmers, Y. J. Chen, A. K. Pymer, Z. H. Loh, S. G. Sayres, S. Pabst, R. Santra, and S. R. Leone, Nat. Phys. **13**, 472 (2017).
28. M. X. Wu, S. H. Chen, S. Camp, J. K. Schafer, and B. M. Gaarde, J. Phys. B **49**, 062003 (2016).
29. M. Reduzzi, J. Hummert, A. Dubrouil, F. Calegari, M. Nisoli, F. Frassetto, L. Poletto, S. H. Chen, M. X. Wu, M. B. Gaarde, K. Schafer, and G. Sansone, Phys. Rev. A **92**, 033408 (2015).